MERIS Cloud-Top Pressure

Algorithm Theoretical Basis Document

ATBD 2.3

Rene Preusker, Rasmus Lindstrot, Jürgen Fischer

Free University Berlin
Institute for Space Science

Contents

1 Introduction

Clouds determine the amount of solar radiation scattered back into space as well as they block the terrestrial radiation from the earth's surface. An increase in globally averaged cloud-top height of 1 km results in 1.2K increase in surface temperature (Ohring and Adler, 1978). Furthermore, a 1% change in cloud cover is estimated to have more than twice the effect of a CO_2 doubling (Ramanathan *et al*., 1989). The most important cloud properties with respect to global climate change are the cloud amount, the cloud-top height, the cloud optical thickness and the size of cloud droplets. However, only global observations of the cloud properties may serve global circulation model studies with sufficient input parameters to make them more realistic.

The most precise method for the detection of cloud-top pressure from present infrared satellite measurements is the *CO_2 slicing technique* (Menzel et al, 1983, 2006). The accuracy of the most advanced techniques to derive cloud-top heights is approximately within 500m. For climate studies and also for the improvement in the retrieval of vertical temperature profiles this accuracy has to be improved significantly.

For the retrieval of cloud-top pressure we propose a method, based on reflected solar radiances of a few nanometers within the oxygen A-band absorption centred at $\lambda=761nm$. This method was first proposed by Yamamoto and Wark (1961). Besides theoretical investigations, airborne measurements have shown that the cloud-top pressure and the cloud optical thickness can be inferred from multi channel measurements of the reflected solar radiation (Wu, 1985; King, 1987; Nakajima and King, 1988; Fischer *et al.,* 1991).

There have been only a few aircraft and satellite experiments for the retrieval of the cloud-top pressure from measurements in the O_2 A-band in the last 20 years. Due to instrumental as well as theoretical problems the errors of the estimated cloud-top pressures were in the same range as other operational techniques. (O'Brien and Mitchel, 1992). Cloud-top pressure was successfully derived from measurements taken from an aircraft (Fischer *et al.,* 1991). The accuracy of the estimated cloud-top height was within 40m above a stratocumulus deck with regard to simultaneously taken LIDAR measurements. Further investigations indicate that cloud-top pressure can globally be achievable within $\pm25hPa$ (Fischer and Kollewe, 1994; O'Brien and Mitchell, 1992, Preusker and Lindstrot, 2009). These results are based on theoretical investigations as well as aircraft measurements above various types of clouds. Additional aircraft measurements, such as those taken during the CIVEX campaign 1995 (Bakan *et al*., 1998), are necessary to study a wide variety of physical effects and to validate detection procedures derived from theoretical calculations.

The most commonly used techniques for the remote sensing of atmospheric properties are based on Look Up Tables or simple regression methods. Artificial neural networks are capable to represent complex multidimensional relationships also. Since Rumelhart and McClelland (1986) introduced a learning scheme for artificial neural networks these techniques have been successfully adapted to remote sensing (Lee *et al.,* 1990; Churnside *et al.,* 1994). Such a technique is applied to interpret multispectral radiances within the O_2A absorption with respect to cloud-top pressure.

2   Background and Algorithm Overview

The approach of satellite-borne, O_2 A band-based cloud-top pressure measurements is illustrated in Figure 1. The sunlight reaching the cloud-top is backscattered and a part finally reaches the sensor on board a satellite. For a well mixed atmospheric gas like oxygen and a known vertical profile of the pressure and the temperature the traversed air mass can be estimated by radiance measurements within an absorption band. For monochromatic light in a non-scattering atmosphere the relation between the amount of absorption and the traversed air mass can be described by Lamberts law.

However, this simple approach is not sufficient because it neither includes scattering of radiation inside and outside the cloud nor correctly describes the absorption of non-monochromatic light. The impact of microphysical cloud properties, varying cloud optical thickness, surface albedo as well as the observation geometry on the radiances can be investigated by radiative transfer simulations only. For the development and definition of a cloud-top pressure algorithm the use of radiative transfer models is of advantage for a systematic analysis of the influence of cloud and surface properties as well as of the influence of measurement errors.

Since no simple relationship or analytical formulation of the coherence between the radiances at top of atmosphere and cloud-top pressure exists, radiative transfer simulations are used to establish an appropriate algorithm. There are different mathematical methods to solve the inverse problem. An approach, based on a complete radiative transfer code is not efficient enough with respect to computation time (Kollewe and Fischer, 1994). Faster semi-empirical radiative transfer codes have deficits with respect to accuracy. Several methods provide a solution:

- The use of Lookup Tables which include the simulated radiances for different cloud, atmospheric and surface properties. This method is limited due to the required resolution of the observation geometry and diversity of cloud conditions. A first estimate of the size of such a Lookup Table predicts 300×10^6 cases.
- A polynomial approach such as proposed by Fischer and Graßl (1991) would reduce the size of the required database and the computation times by fitting the dependence between radiances and cloud parameters by polynomials. The coefficients are determined with multi linear regression methods from the results of radiative transfer simulations.
- Neural networks are able to reduce the size of the required database and the computation times drastically. Matrices derived from a supervised learning procedure using simulation results, relate a vector of input information to a vector of cloud properties of interest. They are able to account for the non-linear correlation of the multi spectral radiances, cloud properties and cloud-top pressures.
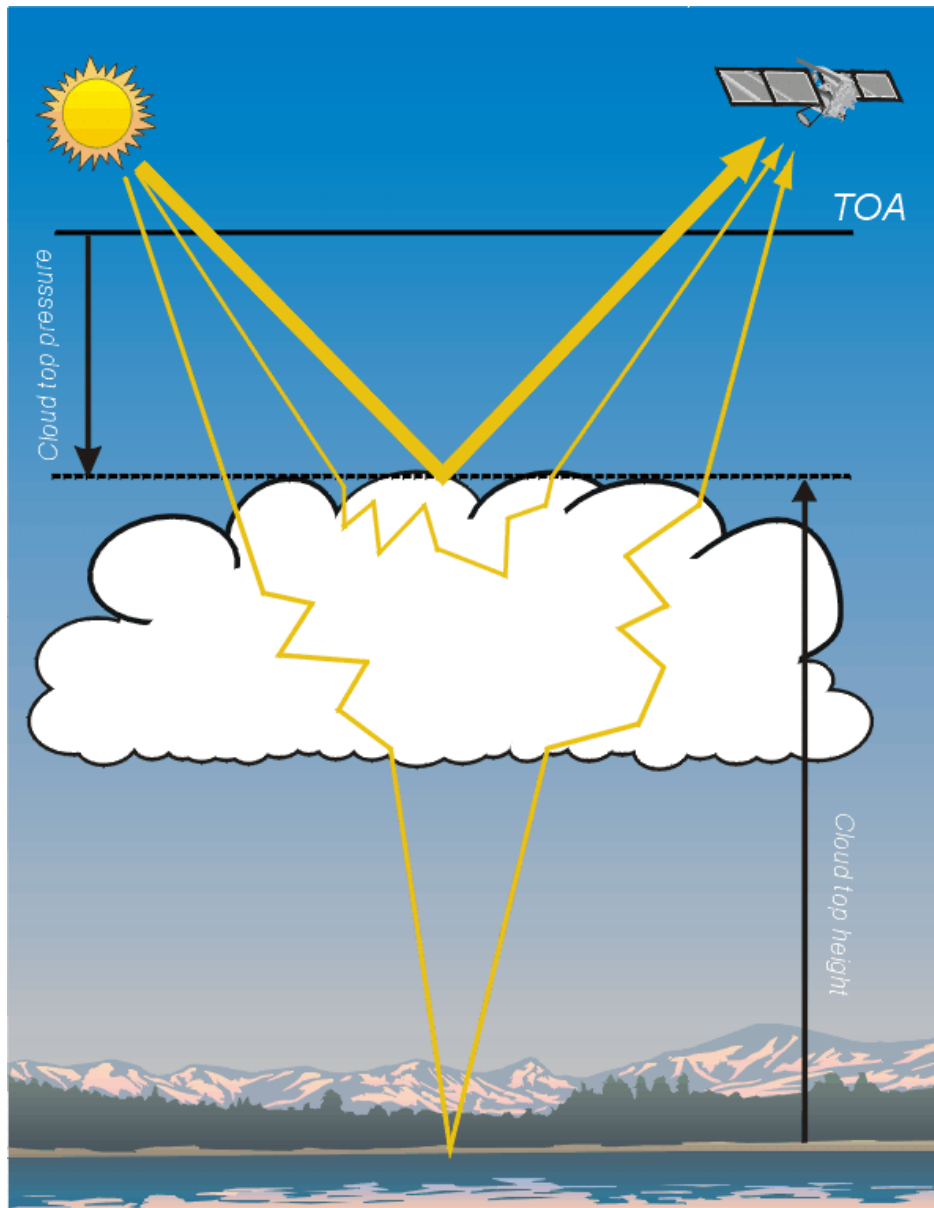
Figure 1 Illustration of the principle of the cloud-top pressure detection using absorption of solar radiation due to well mixed atmospheric gases.

The cloud-top pressure retrieval algorithm dedicated for MERIS uses neural networks. The algorithm can be written as:

$$ctp = \sigma\left(W_{out} \# \sigma\left(W_{in} \# I\right)\right) \qquad (1)$$

where *ctp* is the cloud-top pressure, *W* are the trained weight matrices of the neural net and *I* is the *input vector* containing the measured radiances as well as the viewing geometry and the surface albedo: $I = \left[R_0, R_1, \vartheta_{sun}, \vartheta_{view}, \varphi, \alpha\right]$. # denotes a matrix multiplication and σ symbolises a sigmoidal function.

3   Algorithm Description

3.1   Theoretical Description

3.1.1   Physics of the Problem

The extinction of radiation due to gaseous absorption depends on the absorber mass and on the absorption coefficients within the radiation path. The measured radiance decreases if the photon path within the atmosphere increases. Therefore, the relation between radiances within and outside absorption bands contains information on the absorber mass penetrated by the photons. For a well mixed absorbing gas like oxygen, the total absorption is linear with the total photon path length. The appearance and the position of clouds alter the possible path lengths significantly. Figure 2a and 2b show simulated radiances in the wavelength domain of the O_2A-band for different cloud-top pressures. In both figures the enhanced absorption for lower cloud-top pressures is clearly shown. For a sun zenith angle $\vartheta_0=0^{\cdot}$ and nadir view, there is only a minor dependency of window radiances on cloud-top pressure (Figure 2 upper). For higher sun zenith angles the effects of aerosol and Rayleigh scattering increase and thus lower intensities in window channels for lower cloud-top heights (Figure 2 lower)
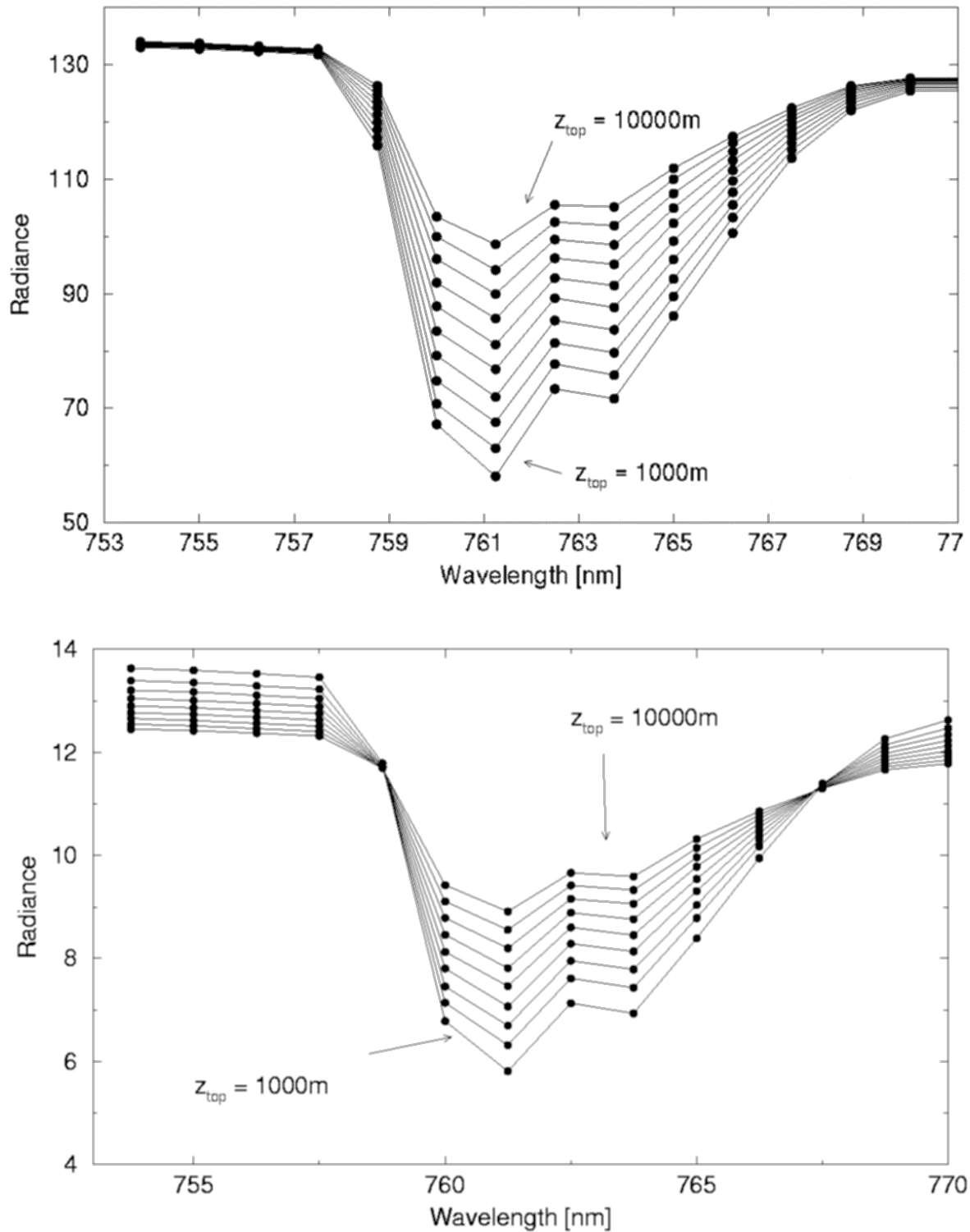
Figure 2: Simulated radiances in the O_2 A-band with different cloud-top pressures. Calculations for solar zenith angle $\vartheta_0=0°$ (upper) and solar zenith angle $\vartheta_0=82.15°$ (lower) and for the cloud parameters: optical thickness $\delta_c=25$, geometrical thickness $\Delta z=1000m$ and effective radius $r_e=8\mu m$. Radiance values in W / m² sr µm.

The vertical profile of a cloud affects the radiances within and outside the oxygen absorption band differently. While radiances in window channels only depend on total optical thickness, radiances within the absorption band are also related to the vertical distribution of liquid water. Photons penetrating into deeper cloud layers have a higher probability of becoming absorbed. In Figure 3 the ratio of simulated radiances at $\lambda=760nm$ and $\lambda=753.75nm$ is shown in a polar plot and a principal plane representation. The left and right side of the Figure belong to the same cloud optical properties and cloud-top pressure but they differ in geometrical thickness of the clouds ($\Delta z=1km$ and $4km$). The ratio of radiances at $\lambda=760nm$ and $\lambda=753.75nm$ is smaller for clouds with a larger geometrical thickness because the photons penetrate into deeper cloud layers.
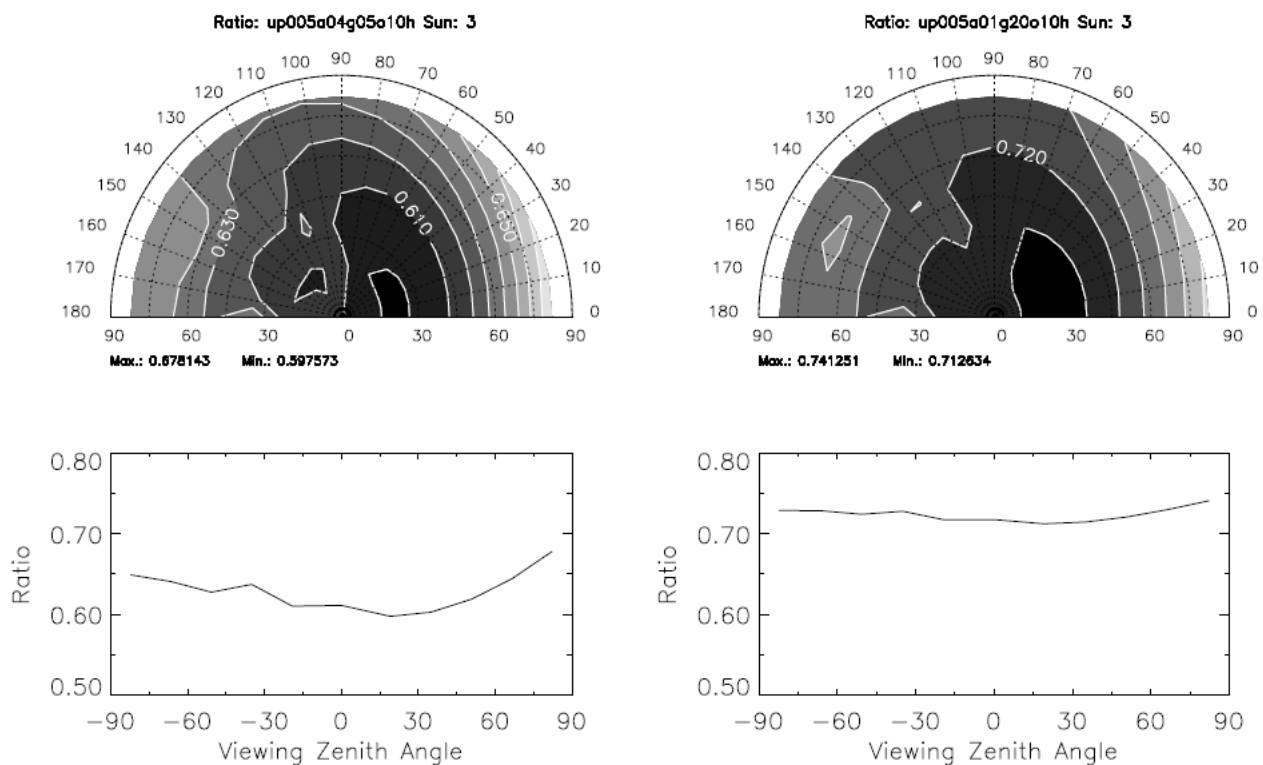

Figure 3: Polar plot and principle plane graph of the simulated field of the ratio between radiances in the O2 A-band at λ =761nm (bandwidth $\Delta\lambda=1.25$ nm) and in the window channel at λ =753.75nm. Calculations are done for solar zenith angle $\vartheta_0=35°$ and for cloud parameters: optical thickness $\delta_c=20$, cloud-top height $z_{top}=10km$ and effective radius $r_e=8\mu m$. The geometrical thickness is $\Delta z=4km$ (left) and $\Delta z=1km$ (right).

The information on the penetration depth is required for a precise cloud-top pressure retrieval. The penetration depth can be taken into account by using additional measurements within the absorption band (Fischer and Graßl, 1991). Depending on the wavelength the absorption in the O$_2$ A-band differ and the radiation penetrates to different depths within the cloud. During the ESA ELAC '90 aircraft campaign 160.000 multi spectral radiance measurements within the O$_2$ A-band were taken with a spectral resolution of 0.4nm above different types of clouds over Europe (Fischer and Kollewe, 1994). According to a multivariate analysis three independent quantities for the cloud-top pressure retrieval could be identified, which are related to three

channels, two within and one outside the absorption band. The photon penetration was found to be the most challenging process to account for and to predict within the retrieval scheme. The vertical distribution and the size of the cloud droplets, expressed by the liquid water content has to be considered within the algorithm. For typical clouds the liquid water content increases with height above the cloud base until a maximum in the upper half is reached (Pruppacher, 1980). Also, the liquid water content of different cloud types such as stratus, stratocumulus and cumulonimbus differ only by a factor of two as long as the temperature does not exceed 280K (Feigelson, 1984). According to this, the variation of liquid water content and its vertical distribution is limited. LWC profiles for different cloud types have to be considered for the development of the cloud-top pressure algorithm.

3.1.2   Mathematical Description of the Algorithm

3.1.2.1 Radiative Transfer Calculations

All approaches for the cloud-top pressure retrieval, as proposed in this document are based on radiative transfer calculations. The radiative transfer code MOMO (Fischer and Graßl, 1984; Fell and Fischer, 2001) is used to simulate the radiances in the MERIS channels. This code assumes a plan parallel atmosphere, however any vertical inhomogenity and media of any optically thickness as well as any spectral resolution can be considered. In order to account for the radiation that is backscattered anisotropically from clouds, the simulations have to be performed for a wide range of observation geometries. In order to account for the required accuracy in cloud-top pressure determination, the model atmosphere is divided into 78 layers.

Since the surface reflection affects the radiance even above thick clouds, variations in surface albedo have to be taken into account. Within the simulations the results of high spectral resolution measurements of various types of surfaces were used (Bowker *et al*., 1985). Different types of vegetation, soil and snow as well as an ocean surface are considered, whereby the albedo and the albedo slope cover natural occurring values. In particular over vegetation the impact of the position of the red edge on the TOA radiances is included. The reflection at the surface is assumed to be isotropic.

A correlated k-distribution method is used to incorporate gaseous absorption (Bennartz and Fischer, 2000). The approximation of transmission functions with exponential sums is used for the spectral integration within the radiative transfer code. This is necessary for the integration of the MERIS channels which are influenced by molecular absorption. The calculation of the gas absorption is based on the HITRAN dataset (Rothman *et al.,* 2009), which contains parameters of the single absorption lines of the main atmospheric gases.

The scattering and absorption processes due to aerosols and cloud particles are represented by appropriate scattering and extinction coefficients and the corresponding scattering phase function. These parameters are obtained by Mie theory (Wiscombe, 1980). The influence of aerosol scattering is almost negligible in cloudy atmospheres, but the simulations distinguish between the *maritime* and *continental* aerosol types with a constant optical thickness of δ_{aero}=0.125 at λ=550nm (Toon and Pollack, 1973; WCP 1986). Sensitivity studies have shown, that the influence of varying cloud droplet size distributions $n(r)$ is only of minor importance for the used cloud-top pressure retrieval algorithm (Fischer and Graßl, 1991). However various

effective radii of cloud droplets were considered. A modified gamma function has been adopted for the cloud droplet size distribution (Hansen, 1971).

The penetration depth in the absorption channels is mainly determined by the relationship between cloud optical thickness, cloud geometrical thickness and cloud-top pressure. Therefore varying combinations of the cloud optical thickness, the vertical profile and the cloud geometrical thickness are considered. The vertical profile of the extinction coefficient is supposed to be 'triangular' whereas the maximum appears in the upper half of the cloud. The optical thickness varies between 1 and 350 while the geometrical thickness varies between 0.1 km and 10 km. In that manner, the variability of penetration depth is considered. Therefore the calculations distinguish different cloud types that are specified through the effective radius and ranges of optical thickness, cloud geometrical thickness, extinction coefficients, cloud-top pressure and cloud base pressure (Table 1). For this investigation 2000 arbitrarily chosen cases are considered.

Table 1: Range of cloud parameters used for the radiative transfer calculations, according to the considered cloud types.

Cloud Type Effective Radius (µm)	Cloud-top Height (m)	Cloud Base Height (m)	Cloud Thickness (m)	Extinction (km^{-1})	Cloud Optical Thickness
stratus I 17	100-1500	30-800	100-500	15-20	2-8
stratus II 10	100-1500	30-800	100-500	15-20	2-8
stratocumulus 17	800-2500	500-2500	250-650	16-24	2-14
stratocumulus 10	800-2500	500-2500	250-650	16-24	2-14
nimbostratus 17	5000-12000	50-2000	3000-9000	20-30	100-250
altostratus 8	4000-7500	3000-6000	500-1500	15-20	8-22
cumulus 25	600-3500	500-2500	300-1000	15-20	8-22
cumulonimbus 33	6000-12000	800-2000	4000-10000	25-35	150-350
altocumulus 8	3500-6500	3000-6000	400-600	16-24	8-22
stratified stratus + altostratus I	4000-7500	30-800	1000-5000	16-24	20-100
stratified stratus + altostratus II	4000-7500	30-800	1000-5000	15-20	20-100

3.1.2.2 Neural Networks

Artificial neural networks are structures composed of individual processing elements called units or neurones. Neurones are connected with each other by links wearing weights. The used type of network consists of a succession of layers of neurones where every neurone of a certain layer is connected to all neurones of the previous and the next layer. The first layer is used as an input layer, the last layer as an output layer. The layers between input and output layer are called

hidden layers. The neurones of the hidden and the output layer transform an incoming signal by applying a sigmoidal function σ:

$$\sigma_t(x) = \frac{1}{1 + e^{-t \cdot x}} \qquad (2)$$

where t is the 'temperature' parameter of the activation function. The connection between the layer n and $n+1$ is represented by the *weight matrix W_n* where each element $w^{i,j}_n$ represents the weight of the connection from the i-th neurone in layer n to the j-th neurone in layer $n+1$. Figure 4 illustrates the structure of a neural network with three layers. For a n layer network the processing can be written as:

$$Output = \sigma(W_n \# \sigma(...\sigma(W_2 \# \sigma(W_1 \# Input))..)) \qquad (3)$$

An input vector is transformed into an output vector by a sequence of linear and non-linear transformations. The linear transformation is a matrix multiplication with W_i denoted by #.
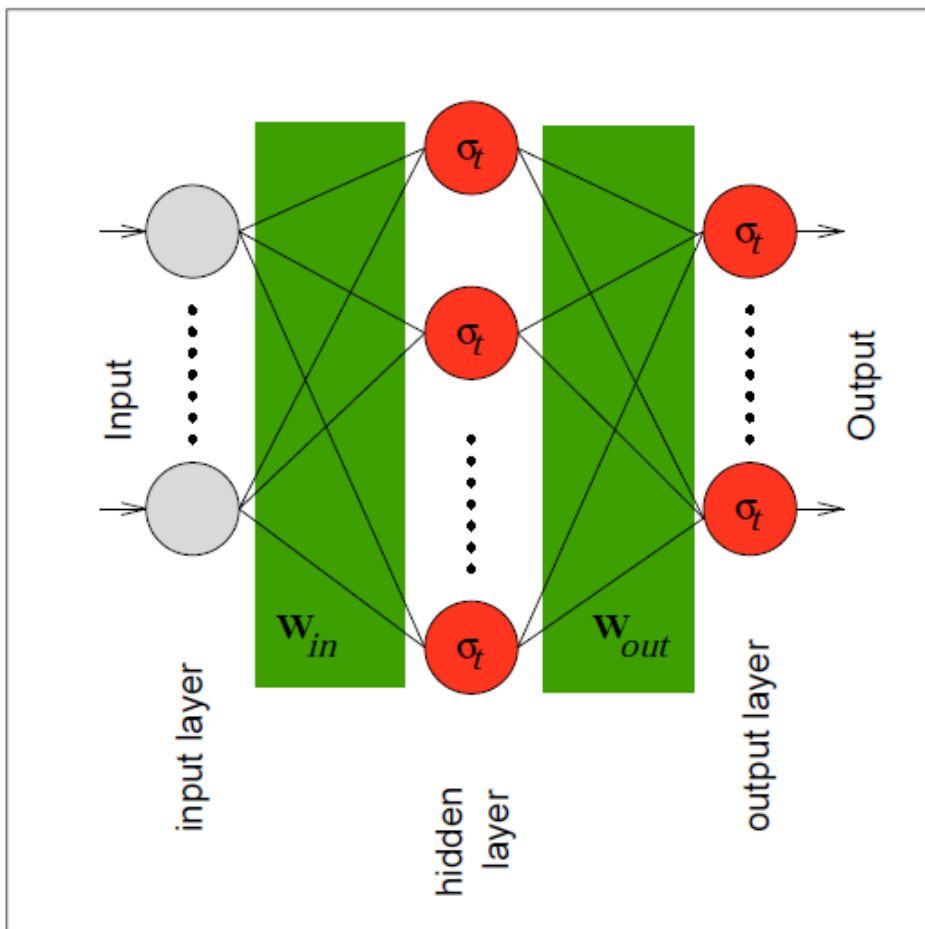

Figure 4: Structure of a neural network with one hidden layer

The neural network learning problem is to find the connection weight matrices W_i. Within the *backpropagation* algorithm it consists of the following steps (Rumelhart, 1986):

1. Initialisation of the matrices with random numbers.
2. Procession of one or more training patterns with the neural net.
3. Calculation of the difference between retrieved output and original output of the training pattern.
4. *Propagation* of the difference *back* through the network and evaluation of the gradients W_cor_i.
5. Correction of the weight matrices by: $W_i = W_i + \gamma \, W\_cor_i$. γ is the learning parameter

Steps 2-5 are performed with all training patterns until weights are found which minimise the over all error for a test data set. An independent test data set is necessary to avoid *overtraining* (Rojas, 1993). In the last years this kind of neural net training has been successfully adapted to remote sensing (Lee *et al.,* 1990; Churnside *et al.,* 1994). As for every other inversion algorithm the choice of the training and test data sets is of major importance to ensure reliable results.

For the cloud-top pressure retrieval a three layer neural network is implemented. The input contains the TOA reflectance of the MERIS Channels 10 (753.75nm) and 11 (760nm) the sun zenith angle, the viewing zenith angle, the azimuth difference, the albedo of the underlying surface, and the central wavelength of MERIS band 11.

3.1.2.3 Inversion

The general form of the retrieval kernel is given in equation (1). The input vector of the neural net contains the reflectance in the MERIS channel 10, 11 and the viewing geometry: sun zenith, viewing zenith and azimuth. Prior to the inversion process, the reflectance of band 11 is corrected for residual stray light, as detailed in section 3.2.3. The In order to account for the influence of the surface reflectance, the albedo is additionally contained in the input vector. Above land surfaces, the surface albedo is taken from the MERIS Albedomap, as outlined in section 3.2.2. Finally, the central wavelength of the pixel under consideration serves as an additional input parameter for the inversion. It is extracted from an auxiliary data base, relating the detector index given in MERIS L1B files to the central wavelength, as outlined in section 3.2.2.

3.2 Practical Considerations

3.2.1 Numerical computation considerations

The size of the matrices for the neural network approach depends on the number of hidden neurones. The optimal number of neurones was found to be 30. This corresponds to a size of 20kB.
The procedure does not contain iterative loops.

3.2.2 Auxiliary data

The MERIS cloud-top pressure algorithm makes use of two auxiliary data sets. The first one is the MERIS albedomap, a global, temporally resolved data base of surface albedo (Muller et al., 2006). I provides global 16-day averages of surface reflectance in the MERIS window channels on a rectangular longitude-latitude grid at a spatial resolution of 0.05°.

The second auxiliary data set provides tables of
- coefficients for the correction of residual, instrumental stray light,
- the centre wavelength of MERIS band 11 depending on the MERIS detector index.

The second auxiliary data set is further detailed in section 3.2.3.

3.2.3 Empirical stray light correction and central wavelength of band 11

Instrumental stray light is caused by multiple scattering and reflection at optical elements within the spectrometer like lenses or gratings. The correction of stray light is particularly important in absorption bands because weak intensities are affected strongly even by small offsets caused by stray radiation. Therefore, the O_2 A-band based algorithms for the retrieval of cloud-top pressure from MERIS is susceptible to errors caused by instrumental stray light. Although there is a correction for stray radiation in the operational MERIS processing chain (MERIS ground segment, Merheim-Kealy et al., 1999), artifacts are apparent in the pressure retrievals in particular, which are likely to be caused by residual stray light. The quantification of the stray light effect on the retrieval errors is complicated by a high correlation with the effect of the spectral calibration uncertainty: a spectral shift of the oxygen A-band channel toward weaker or stronger absorption causes a signal similar to an under- or overestimation of the stray light contribution to the measured radiance. Because the MERIS swath is composed of the measurements of five identical cameras with individual characteristics, the errors induced by stray light and spectral calibration issues become evident particularly at the borders of the field of view of the cameras, resulting in discontinuities of the derived pressure.

In order to assess the residual stray light amounts in MERIS bands 11, the coefficients of a simple, brightness- and viewing angle-dependent stray light model were optimized by adjusting the derived surface and cloud-top pressure to reference data. Along with the stray light correction model, the central wavelength of MERIS band 11 was determined, both by minimizing the deviation of the derived pressure values from the truth.

The effect of the residual stray light is corrected by subtracting a fraction f of the window radiance at 753nm from the radiance in the absorption channel at 761nm. Figure 5 shows an exemplary cloud-top pressure retrieval before and after applying the empirical stray light correction factors. Further details on the empirical stray light correction can be found in Lindstrot et al, 2010.
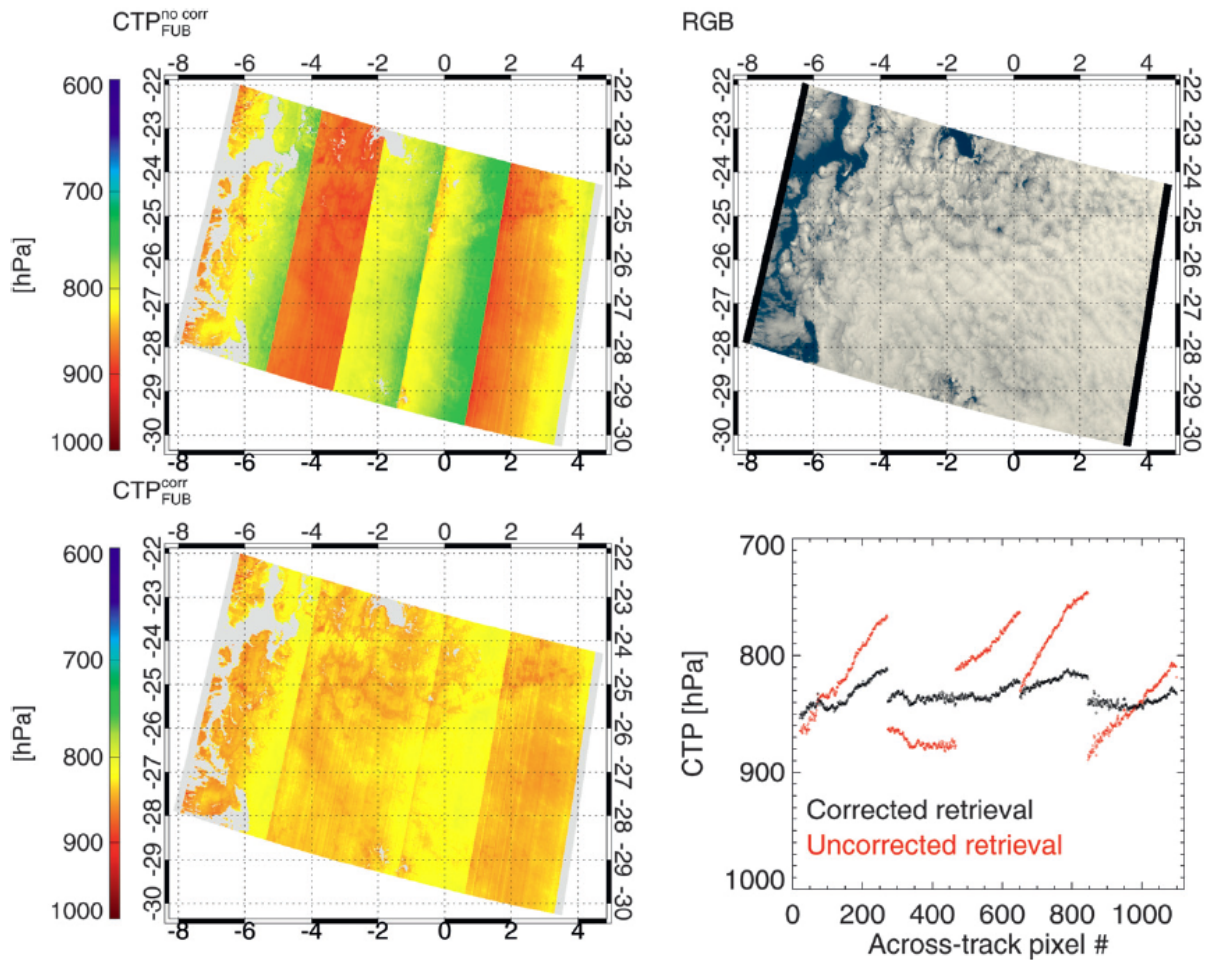
Figure 5: Derived cloud-top pressure before and after stray light correction (left panels) for homogeneous, marine Stratocumulus scene. Along-track median values for complete scene are shown in lower right panel for both retrievals.

3.2.4   Validation

3.2.4.1 MOMO validation

A validation of the MOMO model has been carried out with measurements (Fischer *et al.*, 1991) as well as with other radiative transfer simulations for which good agreements are found (Heinemann and Gentili, 1995; Fell and Fischer, 1995). A comparison of MOMO results with high spectral resolution measurements of OVID is shown in Figure 6. The spectra were recorded during EUCREX '95 above a stratus cloud above the Atlantic in the vicinity of Brest, France. The measured spectrum (average spectrum and standard deviation in the grey area) could be well described with the MOMO model (thick line) when using *in situ* measured cloud particle size distribution (r_e=9μm) and estimated optical thickness (δ_c=20). For the radiances in the

window regions and in the absorption band of water vapour and oxygen we found a very good agreement.
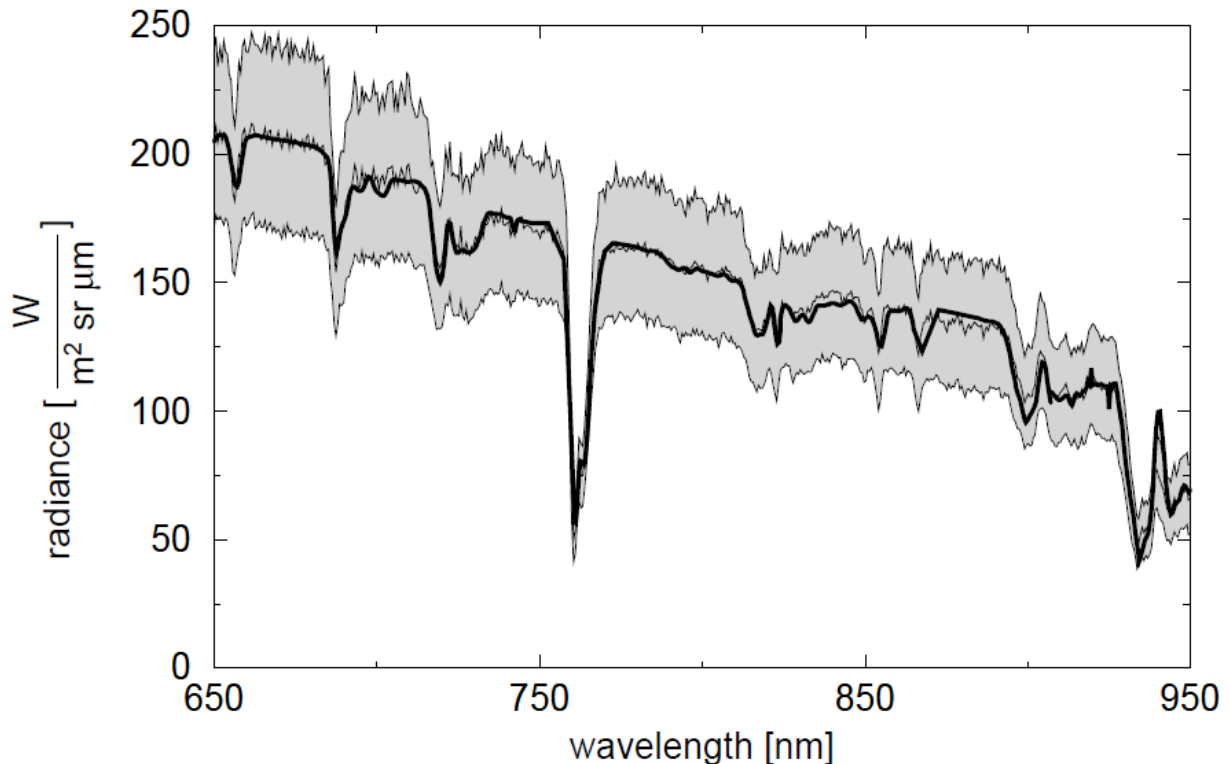

Figure 6: Comparison between measured and simulated radiances above clouds. The averaged measured radiance and its standard deviation is denoted with the shadowed area. The spectra were recorded with the high resolution multi channel spectrometer OVID during EUCREX `94 above a stratocumulus field. The thick line is the simulated spectrum calculated with the cloud parameter $\delta_c=20$, geometrical thickness $\Delta z=600m$, cloud-top height $z_{top}=1100m$ and effective radius $r_e=9\mu m$.

3.2.4.2 Algorithm validation

The MERIS cloud-top pressure algorithm was validated during a validation campaign using airborne LIDAR measurements (Lindstrot et al, 2006).

Twelve validation flights were conducted in the northeastern part of Germany between April and June of 2004. A Cessna 207T of the Freie Universität Berlin served as a measurement platform for the Portable Lidar System (POLIS) of LMU Munich. Figure 7 shows an example of the results for 26 May 2004. The height of the mostly closed, homogeneous Stratocumulus deck was accurately detected by MERIS with deviations between 0 and 300m during the ENVISAT overpass. The small scale variations of the cloud deck are well represented by MERIS.

Similar results were found for all other days with single-layered low level clouds. Higher deviations were observed in cases of cirrus clouds overlapping the low cloud layer.
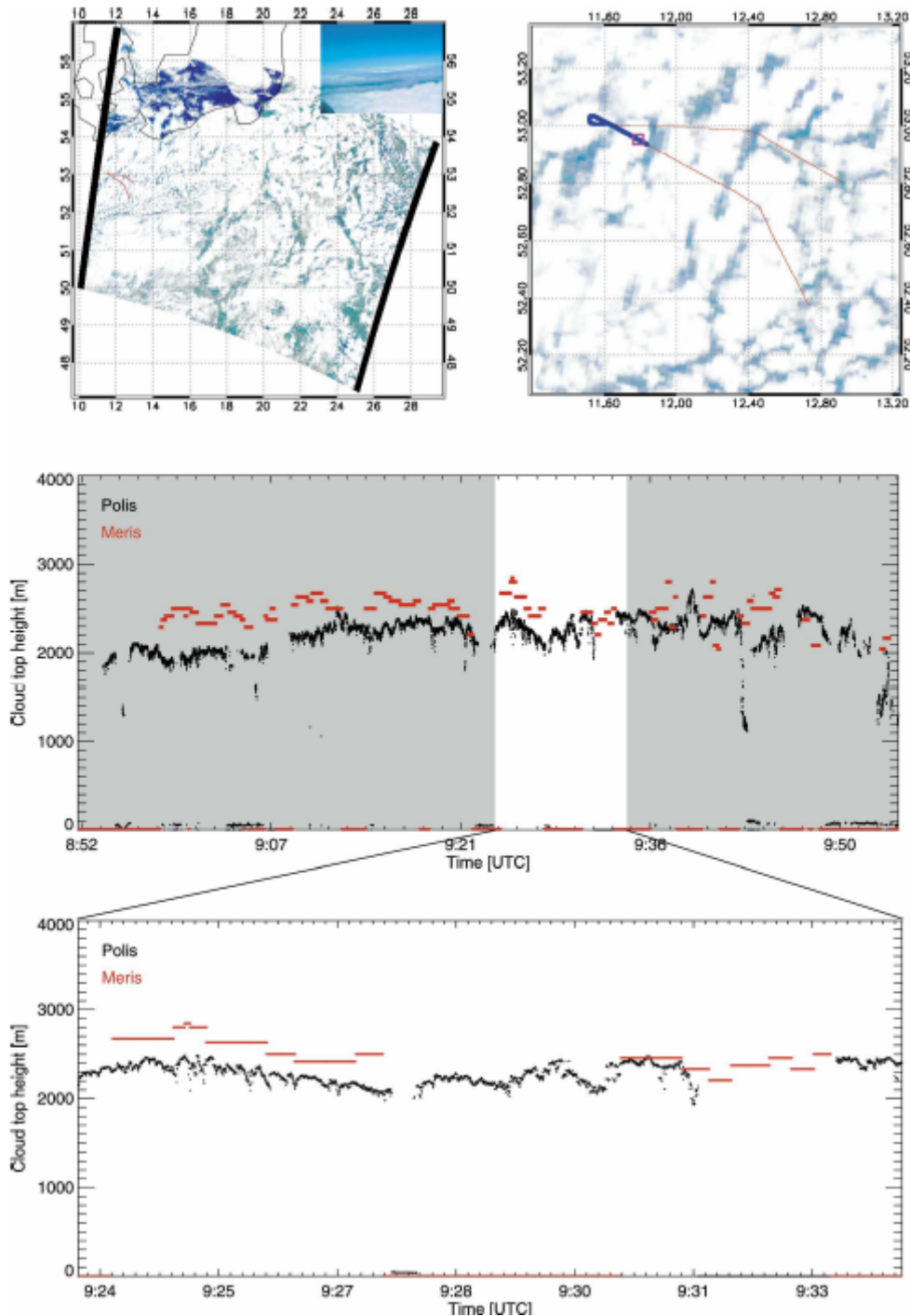
Figure 7: Exemplary comparison of MERIS cloud-top pressure (converted to cloud-top height) with airborne LIDAR measurements on 26 May, 2004. Upper panels show MERIS RGBs with overplotted flight tracks, with the blue parts of the track indicating the ENVISAT overpass time. Lower panels show MERIS measurements in red and POLIS values in black. Grey shaded areas of time series are outside of ±5 minutes of ENIVSAT overpass.

Overall, apart from deficiencies of the MERIS cloud mask and a small, systematic underestimation of cloud-top pressure, the validation campaign revealed a high quality of

MERIS cloud-top pressure for the considered cases. On average, the accuracy was found to be 24 hPa with a bias of -22 hPa in cases of low, single-layered clouds. Figure 8 shows the corresponding scatter plot of MERIS and POLIS cloud-top heights, based on the values found in the time frame of ±5minutes around each ENVISAT overpass.
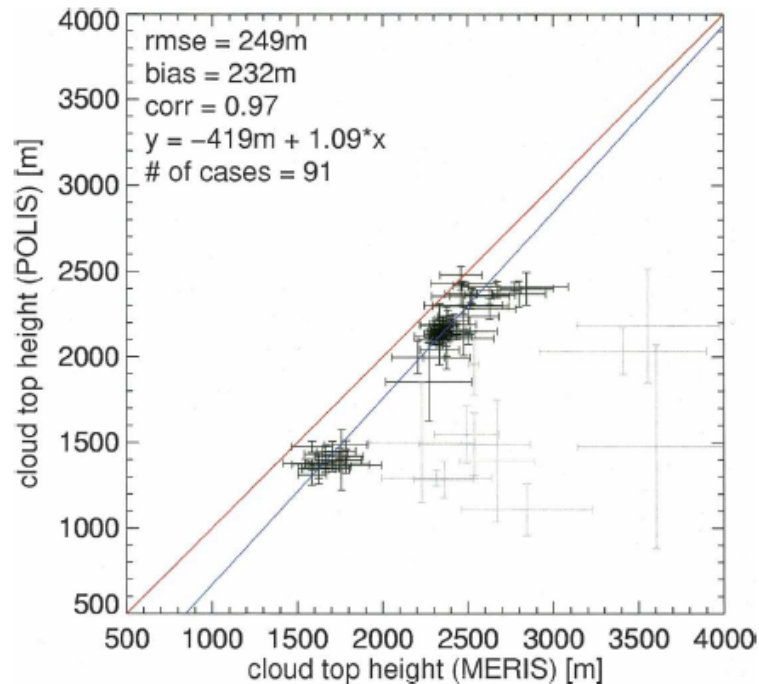

Figure 8: Comparison of POLIS and MERIS cloud-top heights. Grey crosses mark cases with overlapping cirrus clouds (excluded). Error bars are calculated from standard deviation of 10 surrounding MERIS pixels and all POLIS measurement points within the considered MERIS pixel, respectively.

Stronger deviations of the retrieved cloud-top pressure from the true cloud-top can be expected for higher clouds, due to higher variability of the unknown cloud geometrical thickness, influencing the penetration depth of the radiation into the cloud.

The presence of thin cirrus above low clouds leads to a decrease in the accuracy of MERIS CTP because of the effect of the cirrus on the average photon path length. In cases of overlapping cloud layers, the retrieval is thus biased towards a level located between the cloud layers, provided that the upper cloud layer is optically thicker than ≈ 0.5 (see grey crosses in Figure 8).

3.2.5   Quality Control, Diagnostics and Exception Handling

The sensitivity tests for the algorithms indicate measurement situations and measurement errors for which the algorithm is less reliable. The algorithm is applied only for pixels that are indicated as cloudy by the cloud screening algorithm. Pixels for which the quality control failed, will pass the algorithm without result.

If the algorithm receives or retrieves parameters, that lies outside realistic boundaries (defined by the radiative transfer calculations), a quality flag will be raised, indicating, what bond was exceeded. For that specific pixel, no cloud parameter is estimated.

3.2.6 Output Product

The output of the neural is the cloud-top pressure in hPa.

4 Error Budget Estimates and Sensitivity Tests

The ill posed nature of the inversion as well as the shortcomings of radiative transfer modelling and instrumental characteristics affect the accuracy of the cloud-top pressure algorithm. Sensitivity studies on the influence of these errors have been performed to acquire the most sensitive properties of the algorithm. The rmse and the bias are used to characterise the accuracy.

$$rmse = \sqrt{\frac{\sum_{i=1}^{n}\left(ctp_{true} - ctp_{retrieved}\right)^2}{n}} \qquad (4)$$

$$bias = \frac{\sum_{i=1}^{n}\left(ctp_{true} - ctp_{retrieved}\right)}{n} \qquad (5)$$

4.1 Sensitivity to band setting and to spectral registration

The spectral mislocation of the channels can significantly influence the accuracy of the retrieved cloud-top pressure. The O_2 A-band absorption causes a strong sensitivity especially of Channel 11. The spectral mislocation varies from column to column and depends on the relative viewing angle (Figure 9). The mislocation cannot be avoided thus its influence had to be considered in the algorithm.

The optimal spectral location of MERIS band 11 is around 761.75nm, since it provides the highest possible sensitivity to cloud-top pressure and the lowest sensitivity to spectral shifts (Preusker and Lindstrot, 2009). However, due to the spectral smile effect, the actual centre wavelength roughly varies between 760.5 and 762.5nm, resulting in increased susceptibility to uncertainties in the spectral characterization of the instrument.
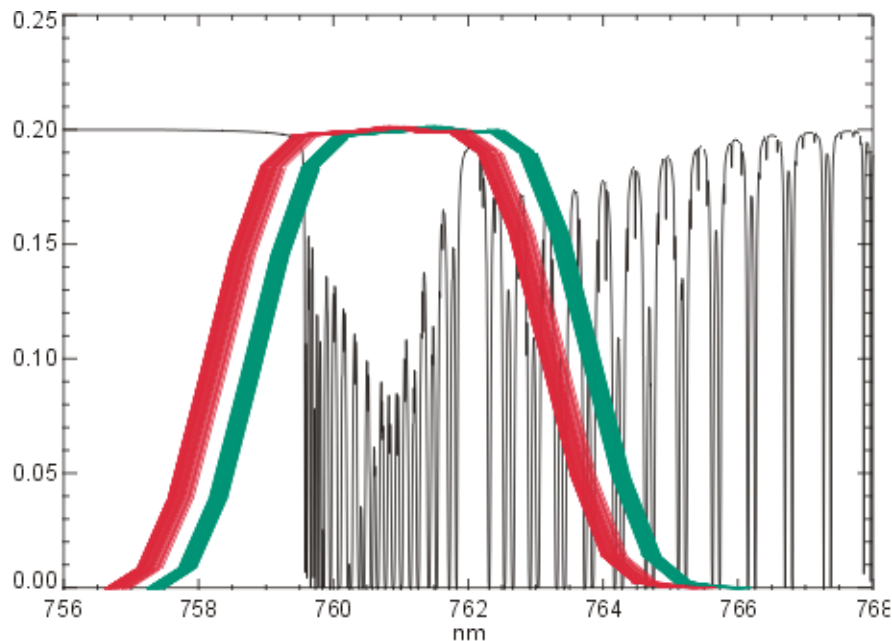
Figure 9: Spectral response functions of several MERIS pixels of channel 11 together with the transmission of oxygen. The green curves belong to camera 3 and the red curves belong to camera 5. The variation within one camera is due to the variability of the channel response within the field of view of a camera ('smile effect').

4.2 Classification of the cloud-top pressure algorithm error

All investigations described in the following sections have been made for an instrumental gaussian noise of 0.5% to account for realistic conditions. Additionally they have been repeated for a band-setting of +/-0.1nm. The results show absolutely no differences to the nominal channel definition. Therefore an algorithm that account for the spectral mislocation is able to neutralise this effect.

4.2.1 Sensitivity to surface albedo and cloud optical thickness

The influence of the surface to the reflectance at top of atmosphere and therewith the accuracy of the cloud-top pressure algorithm increased with decreasing cloud optical thickness and increasing surface reflection. Especially a combination of thin clouds over bright surfaces leads to an overestimation of the cloud-top pressure and thereby to an increasing algorithm error. For moderate optical thickness and surface albedo the bias is neglectable. The rmse is below 30hPa for most the cloud and surface reluctance usually occur. This is due to the ambiguity of the inverse problem according to cloud optical thickness, surface albedo and penetration depth. (Figure 10)
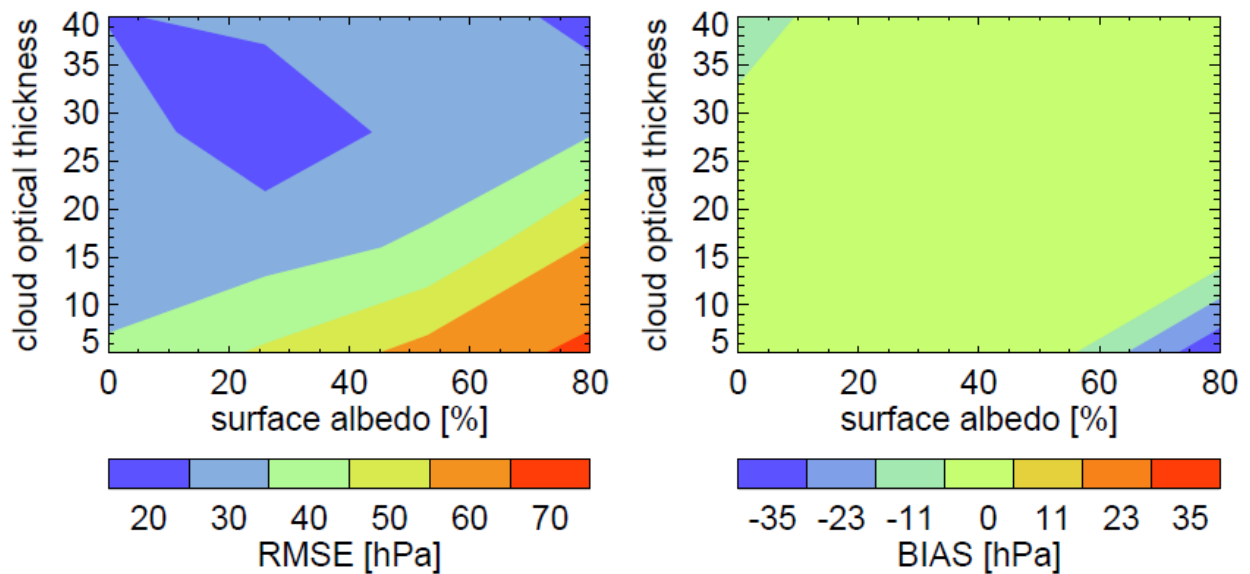
Figure 10: Sensitivity of the ctp algorithm to cloud optical thickness and surface albedo. A negative bias (blue) means overestimation of the cloud-top pressure.

Since the surface albedo can only be known to a certain accuracy the surface albedo of the test data was varied to study this influence. Errors in the albedo of up to 0.2 (rmse) have been simulated.(Figure 11) Again thin clouds and bright surfaces are the most sensitive conditions. Considering that the natural occurrence of thin clouds is higher than of thick clouds the precise knowledge of the surface albedo is a key factor for the ctp accuracy.
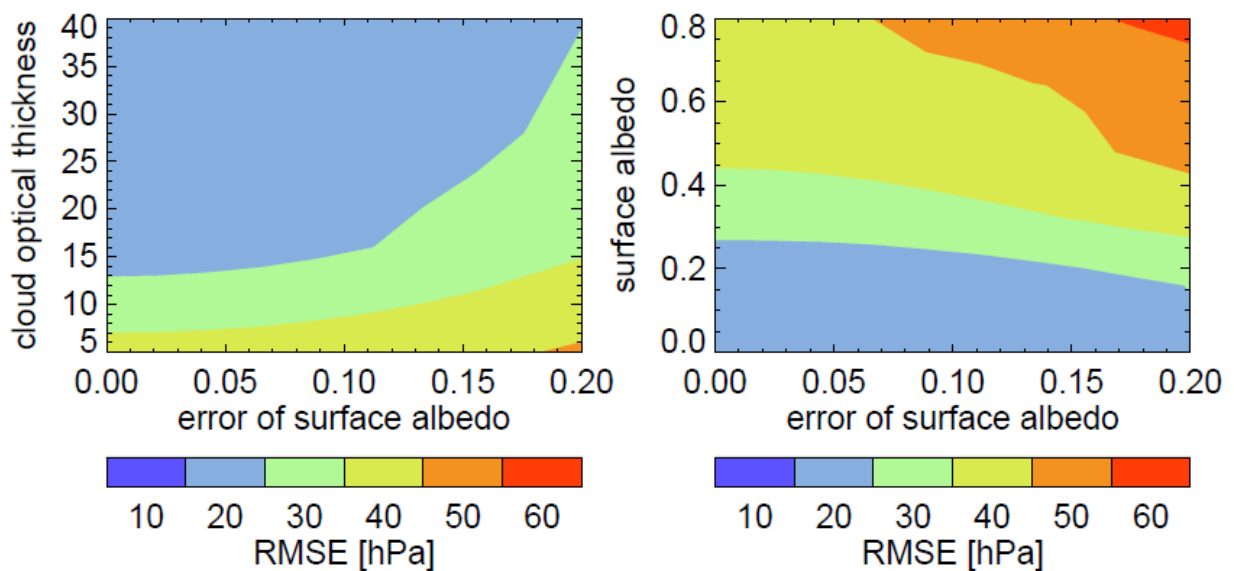

Figure 11: Sensitivity of the ctp algorithm to the error of the surface albedo as a function of the cloud optical thickness (left) and the surface albedo (right).

4.2.2 Sensitivity to cloud optical thickness and cloud-top pressure

As outlined in the last section the accuracy of the ctp algorithm decrease with decreasing cloud optical thickness since the influence of the surface increases. The impact is different for different cloud-top pressures. The cloud-top pressure of low thin clouds will be underestimated in contrary to higher (between 800 hPa and 700 hPa) thin clouds which will be overestimated (Figure 12 right). As in the previous section the reason is the ambiguity of the inverse problem according to cloud optical thickness, surface albedo and penetration depth. This leads to an rmse of the retrieved ctp of up to 55 hPa (red areas in Figure 12 left), which is substantially higher than the overall rmse of 33hPa.
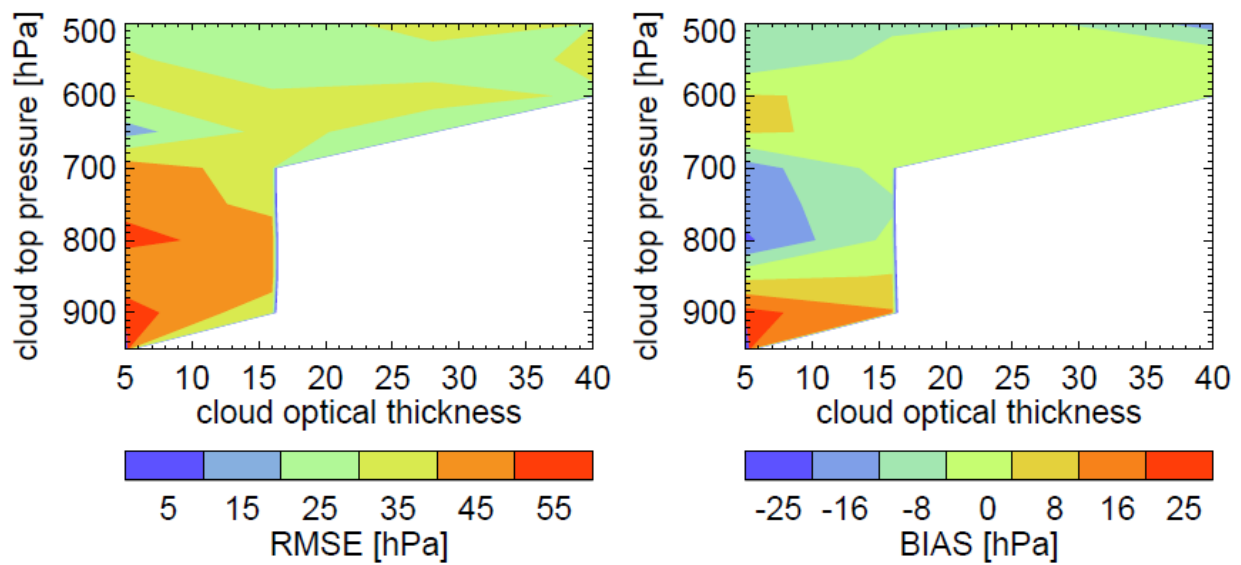

Figure 12: Sensitivity of the cloud-top pressure retrieval to cloud optical thickness and cloud-top pressure. The white areas are not represented in the test and training database.

4.2.3 Sensitivity of the cloud-top pressure retrieval to viewing and solar zenith angle
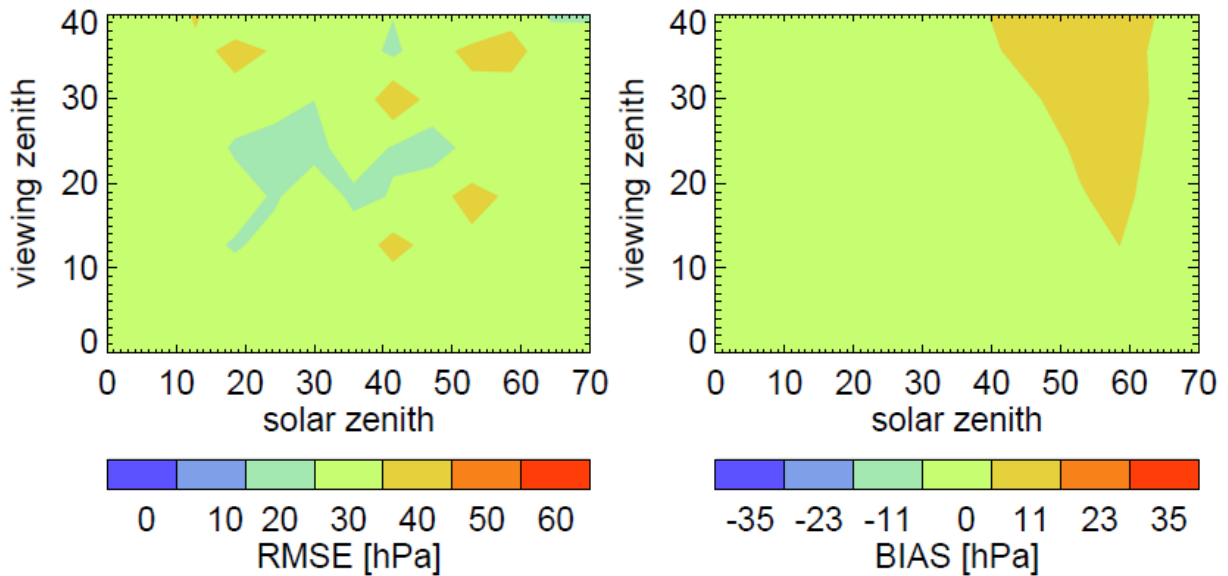

Figure 13: Sensitivity of the cloud-top pressure retrieval to viewing and solar zenith angle.

Figure 13 shows the rmse and the bias of the retrieved cloud-top pressure as a function of the viewing zenith and the solar zenith angle. The rmse has no significant dependence on the viewing geometry whereas the bias shows increases towards high solar zenith and viewing zenith angles.

5 Assumptions and Limitations

The algorithm is based on radiative transfer calculations for which a plan parallel atmosphere is assumed. For low sun elevations and high observation angles, the assumption of a plan parallel atmosphere is less fulfilled. Except for the Monte-Carlo method, there are no 3-dim radiative transfer codes available which could describe the shape of the clouds more realistically. Nevertheless such radiative transfer codes have also significant limitations to describe 3-dim clouds adequately.
Effects from non-horizontal homogenous clouds cannot be treated with the MOMO model, but the influence of vertical distribution of cloud appearance are described. The environment effects of neighbouring pixels cannot be treated with the MOMO model.

6 References

Bakan *et al.* , 1998: CIVEX Field Phase Report

Bennartz, R., and J. Fischer, 2000: A modified k-distribution approach applied to narrow-band water vapour and oxygen absorption estimates in the near infrared. J. Quant. Spectrosc. Radiat. Transfer, 66, 539–553.

Brenguier, J.-L., H. Pawlowska, L. Schüller, R. Preusker, J. Fischer, Y. Fouquart, 1999:Radiative properties of boundary layer clouds: optical thickness and effective radius versus geometrical thickness and droplet concentration, submitted to *J. Atmos. Sci.*

Churnside, J. H., T. A. Stermitz, J. A. Schroeder, 1994: Temperature Profiling with neural network inversion of microwave radiometer data. *J. Atm. Oc. Tec.*, **11**, 105 -109.

Feigelson, E. M., 1984: Radiation in a cloudy atmosphere, D. Riedel Publishing Company, Dordrecht

Fell, F., and J. Fischer, 2001: Numerical simulation of the light field in the atmosphere–ocean systemusing thematrix-operator method. J. Quant. Spectrosc. Radiat. Transfer, 3, 351–388

Fischer, J., and H. Grassl, 1984: Radiative transfer in an atmosphere–ocean system: An azimuthally dependent matrix-operator approach. Appl. Opt., 23, 1032–1039.

Fischer, J., and H. Graßl 1991: Detection of Cloud-Top Height from Backscattered Radiances within the Oxygen A-Band - Part 1: Theoretical Study.- *J. Appl Met.*, **30**, 1245-1259

Fischer, J., W. Cordes, A. Schmitz-Peiffer, W. Renger and P. Mörl, 1991: Detection of Cloud-Top Height from Backscattered Radiances within the Oxygen A-Band Part 2: Measurements. *J. Appl Met.*, **30**, 1260-1267.

Fischer, J. and M. Kollewe, 1994: Study of cloud top height determination using a coarse spatial resolution imaging spectrometer.- Final Report, ESA-ESTEC study, RFQ/3- 7241/91/NL/ BI.

Heinemann, Th. and B. Gentili, 1995: Comparison between Radiances calculated by the Villefranche Monte-Carlo Model and the Berlin Matrix-Operator-Model (MOMO), WP 5000 Radiative Transfer Simulations Preliminary Report

King, M. D., 1987 Determination of scaled optical thickness of clouds from reflected solar radiation measurements. *J. Atmos Sci.*, **44**, 129-144

Lee, J., R.C. Wegner, S.K. Sengputa, and R.M. Welch, 1990: A neural network approach to cloud classification.- *IEEE Transactions on Geoscience and Remote Sensing*, **28** (5), 846-855

Lindstrot, R., R. Preusker, T. Ruhtz, B. Heese, M. Wiegner, C. Lindemann, and J. Fischer, 2006: Validation of MERIS Cloud-Top Pressure Using Airborne Lidar Measurements. *J. Appl. Meteor. Climatol.,* **45**, 1612–1621.

Lindstrot, R, Preusker, R. and Fischer, J., 2010: The empirical correction of stray light in the MERIS oxygen A band channel, *J. Atmos. Oceanic Technol.,* **27 (7)**, 1185-1194.

Menzel, W. P., W. L. Smith, and T. R. Stewart, 1983: Improved cloud motion wind vector and altitude assignment using VAS. J. Climate Appl. Meteor., 22, 377–384.

Menzel, W. P., R. A. Frey, B. A. Baum, and H. Zhang, 2006: Cloud-top properties and cloud phase algorithm theoretical basis document. Cooperative Institute for Meteorological Satellite Studies, Algorithm Theoretical Basis Doc. MOD04, 62 pp.

Merheim-Kealy, P., J. P. Huot, and S. Delwart, 1999: The MERIS ground segment. Int. J. Remote Sens., 20, 1703–1712.

Muller, J.-P., R. Preusker, J. Fischer, M. Zuhlke, C. Brockmann, and P. Regner, 2007: ALBEDOMAP: MERIS land surface albedo retrieval using data fusion with MODIS BRDF and its validation using contemporaneous EO and in situ data products. Proc. IGARSS Int. Geoscience and Remote Sensing Symp., Barcelona, Spain, Institute of Electrical and Electronics Engineers, 2404–2407.

Nakajima, T., M. D. King, 1988: Cloud optical parameters as derived from multispectral cloud radiometer. Vale, FIRE Science Experiment Team

Neckel, H. and D. Labs, 1984 Improved Data for Solar Spectral Irradiance from 330 to 1250nm, *Solar Phys.*, **90**, 205-258

O'Brien, D. and R.M. Mitchell, 1992: Error estimates for Retrieval of Cloud-Top Pressure Using Absorption in the A Band of Oxygen. *J. Appl. Meteor.*, **31**, 1179-1192.

Ohring, G. and S. Adler, 1978 Some experiments with a zonally averaged climate model, J. *Atmos. Sci.*, **35**, 186-205

Preusker, R., and R. Lindstrot, 2009: Remote Sensing of Cloud-Top Pressure Using Moderately Resolved Measurements within the Oxygen A Band—A Sensitivity Study. *J. Appl. Meteor. Climatol.*, **48**, 1562–1574.

Pruppacher, H. R. 1980 Microstructure of atmospheric clouds and precipitation. *Clouds: Their Formation, Optical Properties adn Effects*, P. Hobbs and A. Deepack, Eds. 93-185

Ramanathan, V., R. D. Cess, E. F. Harrison, P. Minnis, B. R. Barkstrom, E. Ahmad, D. Hartmann, 1989 Cloud radiative forcing and climate: Results from the Earth Radiation Budget Experiment. *Science*, **243**, 57-63

Rojas, R. : Theorie der neuronalen Netze: eine systematische Einführung. Berlin, Springer 1993

Rothman, L.S., I.E. Gordon, A. Barbe, D.C. Benner, P.F. Bernath, M. Birk, V. Boudon, L.R. Brown, A. Campargue, J.-P. Champion, K. Chance, L.H. Coudert, V. Dana, V.M. Devi, S. Fally, J.-M. Flaud, R.R. Gamache, A. Goldman, D. Jacquemart, I. Kleiner, N. Lacome, W.J. Lafferty, J.-Y. Mandin, S.T. Massie, S.N. Mikhailenko, C.E. Miller, N. Moazzen-Ahmadi, O. Naumenko, A.V. Nikitin, J. Orphal, V.I. Perevalov, A. Perrin, A. Predoi-Cross, C.P. Rinsland, M. Rotger, M. Simecková, M.A.H. Smith, K. Sung, S.A. Tashkun, J. Tennyson, R.A. Toth, A.C.

Vandaele, and J. Vander Auwera, 2009: The *HITRAN* 2008 molecular spectroscopic database, JQSRT, **110**, 533-572.

Rumelhart, D. and J. McClelland, 1986 Parallel Distributed Processing. MIT Press, Cambridge, Massachusetts

Toon, O. B. and J. B. Pollack, 1973 A global Average Model of Atmospheric Aerosols for Radiative Transfer Calculations, *J. Appl. Met*, **15**, 225-246

Yamamoto G., D. Q. Wark, 1961 Discussion of the Letter by R. A. Hanel, Determination of Cloud Altitude from a Satellite´. *J. Geophy. Res*, **66**, 3596

WCP-report No. 112, 1986 A preliminary cloudless Standard Atmosphere for Radiation Computation, WMO/TD-No. 24

Wiscombe, W. J., 1980 Improved Mie scattering algorithm, *Appl. Opt*., **19**, 15505-1515

Wu, M.-L. C., 1985 Remote Sensing of Cloud-Top Pressure Using Reflected Solar Radiation in the Oxygen A-Band, *J. Appl. Met*., **24**, 549-546

Product Name: Cloud-top pressure
Product Code: MERIS.RRGCTP
Product Level: Level 2
Description of Product: Cloud-top pressure

Product Parameters:
Coverage   global Packaging
Half-orbit   Units   [hPa]
Range   1050 hPa to 100 hPa   (for polar stratospheric clouds: 50 hPa)
Sampling   pixel by pixel

Resolution   radiometric: Wm-2sr-1µm-1
                         spatial: 1.2km (0.3km)
Accuracy   radiometric: 2-4% (within precision of calibration)
                         geophysical product: 30 hPa
Geo-location requirements 1-4 pixels, depending on use of cloud-top pressure
                         Format 16 bits / sample (TBC)
Appended Data   Earth location, Quality mask (i.e. residual of inversion process)
Frequency   1 product per orbit
Size of Product   TBD

Additional Information:
Identification of bands used in algorithm: l=753.75 nm, l =760 nm
Assumptions on MERIS input data: None
Identification of ancillary and auxiliary data: surface albedo, stray light correction coefficients,
MERIS band 11 central wavelength
Assumptions on ancillary and auxiliary data: TBD
Input from other ENVISAT instruments: None